PCCP

PAPER



Cite this: *Phys. Chem. Chem. Phys.*, 2023, **25**, 11707

# Marangoni- *vs.* buoyancy-driven flows: competition for spatio-temporal oscillations in A + B → C systems†

Adam Bigaj, *[a] Marcello A. Budroni, *[b] Darío Martín Escala [a] and Laurence Rongy *[a]

Received 9th February 2023,
Accepted 28th March 2023

DOI: 10.1039/d3cp00637a

rsc.li/pccp

The emergence of self-organized behaviors such as spatio-temporal oscillations is well-known for complex reactions involving nonlinear chemical or thermal feedback. Recently, it was shown that local oscillations of the chemical species concentration can be induced under isothermal batch conditions for simple bimolecular A + B → C reactions, provided they are actively coupled with hydrodynamics. When two reactants A and B, initially separated in space, react upon diffusive contact, damped spatio-temporal oscillations could develop when the surface tension increases sufficiently in the reaction zone. Additionally, if the density decreases, the coupling of both surface tension- and buoyancy-driven contributions to the flow can further sustain this oscillatory instability. Here, we investigate the opposite case of a reaction inducing a localized decrease in surface tension and an increase in density in the reacting zones. In this case, the competition arising from the two antagonistic flows is needed to create oscillatory dynamics, *i.e.*, no oscillations are observed for pure chemically driven Marangoni flows. We study numerically these scenarios in a 2-dimensional system and show how they are controlled by the following key parameters: (i) $\Delta M$ and $\Delta R$ governing the surface tension and density variation during the reaction, respectively, (ii) the layer thickness of the system, and (iii) its lateral length. This work is a further step toward inducing and controlling chemical oscillations in simple reactions.

## 1 Introduction

When a system is kept out of equilibrium, ordered structures and self-organized behaviors can emerge.[1] Under these conditions chemical systems are governed by their kinetics and, if this involves nonlinear chemical or thermal feedback, dynamics as complex as autonomous oscillations can occur.[2–4] Complicated temporal behaviors like periodic or chaotic dynamics are not the only possibility and, in spatially extended systems, the interplay between oscillatory kinetics and transport phenomena can bear the formation of travelling waves and structures.[5]

The famous Bray–Liebhafsky[6] or Belousov–Zhabotinsky[7] reactions are now classical examples of such a class of reactions which represent a sort of inorganic model systems for complex oscillatory dynamics encountered in the biological world, such as metabolic cycles, calcium signaling, circadian rhythms or morphogenesis, to name a few.[8,9]

Apart from the understanding and imitation of biological functional behaviors, oscillatory dynamics find application in a large variety of fields including the design of new smart materials, like self-oscillatory polymers or gels.[10] These are typically chemo-responsive materials that, coupled to chemical oscillators, can show periodic volume variations (chemo-mechanical oscillations) which can be exploited for the delivery of drugs at controlled time lapses, to actuate autonomous locomotion and to design chemorobots.[10–13] Networks of chemical oscillators, where autonomous self-oscillators are encapsulated in confined domains, were also employed to mimic neuron behaviors and unveil how their communication gives rise to collective dynamics and different synchronization patterns on the basis of functional activity.[14–18] This represents the ground for the development of chemical computing (so-called wetware) and chemical artificial intelligence,[19] recently applied to unconventional diagnosis of schizophrenia and some kind of cancers.[20,21] The mastery developed in nonlinear chemical phenomena has also been applied to control and optimize relevant processes for the production of alternative green sources of energy, like molecular hydrogen from borohydrides.[22]

[a] *Nonlinear Physical Chemistry Unit, Service de Chimie Physique et Biologie Théorique, Université libre de Bruxelles (ULB), CP 231 – Campus Plaine, 1050 Brussels, Belgium. E-mail: adam.bigaj@ulb.be, laurence.rongy@ulb.be; Fax: +32 (0)2 650 5767; Tel: +32 (0)2 650 5699*

[b] *Department of Chemistry and Pharmacy, University of Sassari, Via Vienna 2, 07100 Sassari, Italy. E-mail: mabudroni@uniss.it*

† Electronic supplementary information (ESI) available. See DOI: https://doi.org/10.1039/d3cp00637a

Most of the oscillatory dynamics considered in these different fundamental and applied studies are limited to the realm of nonlinear chemical reactions. However, a parallel line studying the occurrence of complex behaviors in systems governed by simple reactions has attracted increasing interest in recent years.[23,24]

Boosted by the pioneering work of Gàlfi and Ràcz,[25] reaction-diffusion (RD) fronts in A + B → C systems, whereby two reactants A and B initially separated in space react upon diffusive mixing,[25,26] have been thoroughly studied. If both reactants present equal initial concentrations and diffusion rates, the bimolecular RD front remains localized at its initial position and develops symmetrically. However, as a small difference in the initial concentrations of the reactants and/or diffusion rates is introduced, the front propagates in time toward preferential directions.[27,28]

It was shown that these simple structures can evolve to unexpected behaviors, for example, when one reactant is sandwiched between two pools of the other one, two A + B → C fronts can interact together in the form of attractive or repulsive collective dynamics, depending on the initial distance between the fronts.[29]

It was recently shown that simple A + B → C reactions can also exhibit spatiotemporal oscillations, provided that the reaction combines with hydrodynamics.[30–33] In reactive fluids, natural convection can indeed arise spontaneously from changes in the composition/temperature of the system, further inducing *in situ* local gradients in the physical properties (*i.e.* density and/or surface tension), thereby activating convective motions within the fluid itself. Convective flows interact, in turn, with the initial RD fronts and new dynamics can develop.[34,35] Both the scenarios in which the reaction induces a flow[35] and when chemical structures like fronts or waves propagate through an established flow field[36–38] have been thoroughly studied.

Oscillatory and wavy dynamics were observed, both numerically[39,40] and experimentally,[41–44] for nonlinear non-oscillatory kinetics. For instance, in the case of autocatalytic fronts, an antagonistic coupling between solute and thermal effects triggers oppositely-oriented buoyancy- or Marangoni-driven flows. Spatio-temporal oscillations were also reported for isothermal conditions in the propagation of an autocatalytic front again due to an antagonistic interplay between Marangoni- and buoyancy-driven convection.[45]

The behavior of already oscillatory kinetics was shown to be further complicated by the onset of chemically-induced convection. This can drive the transition from regular periodic waves to chemical turbulence,[46–48] the development of pulsating and/or traveling hydrodynamic fingering if the oscillator is localized across the mixing area of two stratified solutions containing subparts of the reaction,[49–51] and the enhancement or suppression of chemical oscillations involving an enzymatic component.[52] The potential of hydrodynamics in combination to oscillatory kinetics has even been introduced in neuromorphic engineering, chemical artificial intelligence, and chaos computing.[53,54]

With the objective of designing autonomous self-organized complex behaviors in simple chemical systems (without any internal or external feedback), we will exploit here chemohydrodynamics in combination with an A + B → C reaction. As it was already shown, if a reaction front can locally increase the surface-tension of a solution beyond a certain threshold, transient oscillatory dynamics can develop due to the competition between Marangoni converging flows (front compression) and vertical diffusive relaxation.[30,31] Furthermore, when buoyancy-driven flows combine antagonistically with the Marangoni effect, *i.e.* when the localized reaction increases the surface tension and decreases the density in the mixing zone, the oscillatory mechanism is further enhanced and sustained pulsations can be observed.[30–32]

In this article, we focus on the reverse antagonistic case where the reaction decreases the surface tension of the solution and increases its density, for which a new kind of oscillatory behavior (*e.g.* a bimodal oscillatory dynamics), so far not encountered in bimolecular A + B → C systems, has been identified.[31,32] Section 2 details the model and governing equations. This is followed by a presentation of the oscillatory dynamics in Section 3. The mechanism of the formation and propagation of spatio-temporal oscillations, as well as the role of different key parameters on these dynamics are described before concluding in Section 4.

## 2 Model

We consider a two-dimensional reactor of length $L_X$ and height $L_Z$ in the $(X, Z)$ reference frame, where $Z$ is oriented against the gravitational acceleration $\mathbf{g} = (0, -g)$. The reactor is supposed to be isothermal, closed at the bottom and lateral borders and open at the top border with an air–liquid interface supposed to be non-deformable. We neglect any evaporation. The chemical species concentrations $A$, $B$, $C$ are initially spatially distributed as

$$(A, B, C) = \begin{cases} (A_0, 0, 0) & \text{for } X < X_0 \quad \forall Z, \\ (0, B_0, 0) & \text{for } X > X_0 \quad \forall Z, \\ (A_0, B_0, 0) & \text{for } X = X_0 \quad \forall Z. \end{cases}$$

The reactant solutions A and B, initially separated, react upon diffusive mixing across the contact line localized at the center of the system ($X_0$) and form product C, following the bimolecular A + B → C reaction. In order to simplify the system and to allow for a symmetrical development of the reactive zone, both reactant solutions are assumed to have the same initial surface tension $\gamma_A = \gamma_B = \gamma_R$, density $\rho_A = \rho_B = \rho_R$, and their initial concentrations are considered equal $A_0 = B_0$. The formation of $C$ in the reactive zone induces local changes in the surface tension and density, triggering convective transport in the system [Fig. 1].

The resulting nonlinear dynamics is governed by a set of partial differential reaction–diffusion–convection (RDC) equations,

$$\partial_T A + (\boldsymbol{V}\cdot\nabla)A = D\nabla^2 A - kAB, \quad (1)$$

$$\partial_T B + (\boldsymbol{V}\cdot\nabla)B = D\nabla^2 B - kAB, \quad (2)$$

$$\partial_T C + (\boldsymbol{V}\cdot\nabla)C = D\nabla^2 C + kAB, \quad (3)$$

$$\partial_T \boldsymbol{V} + (\boldsymbol{V}\cdot\nabla)\boldsymbol{V} = -\frac{1}{\rho_0}\nabla P + \frac{\mu}{\rho_0}\nabla^2 \boldsymbol{V} - g\frac{(\rho-\rho_0)}{\rho_0}\mathbf{1}_Z, \quad (4)$$

$$\nabla\cdot\boldsymbol{V} = 0, \quad (5)$$

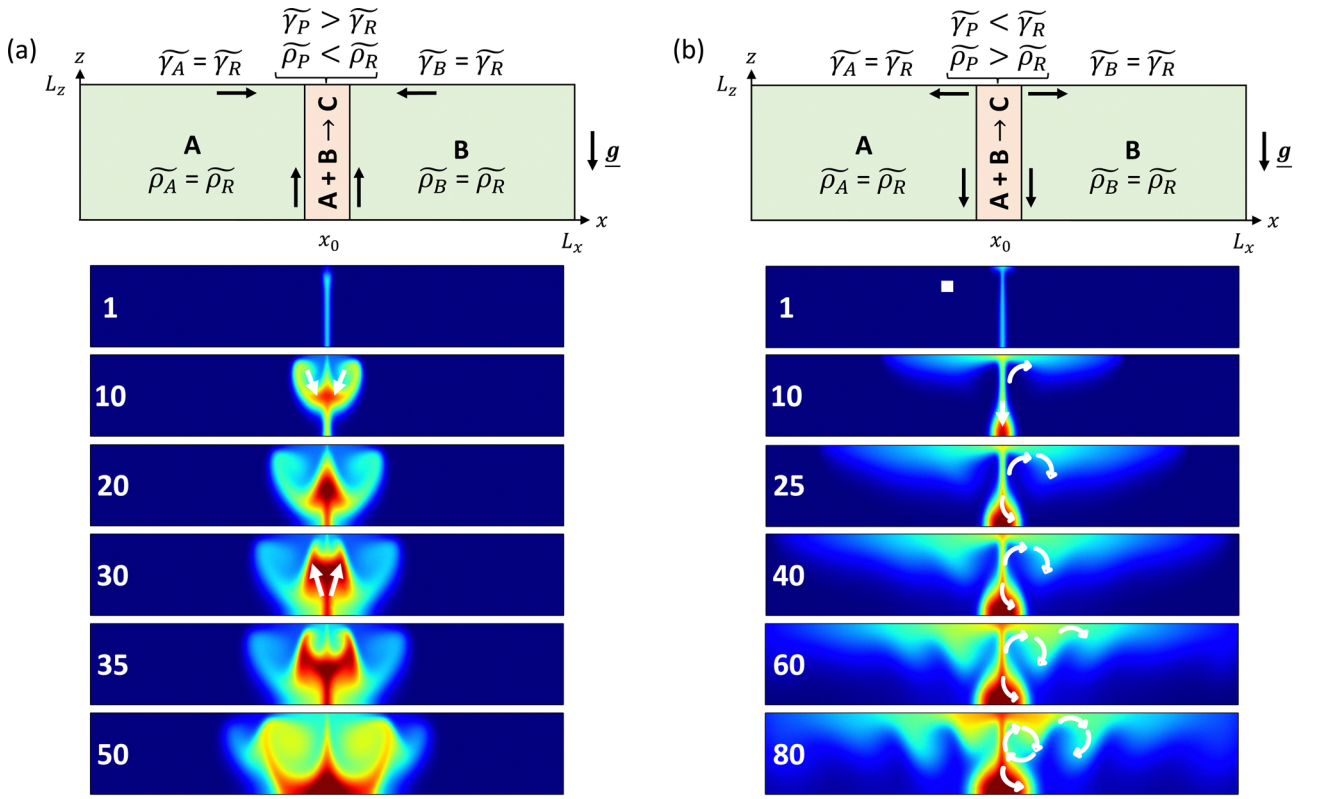


Fig. 1 The top panels represent the sketch of the initial configuration of the A + B → C system. The reactant solutions A and B have the same dimensionless surface tension $\tilde{\gamma}_R$ and density $\tilde{\rho}_R$ and product C forms in the reactive zone, where the reaction (a) increases the surface tension $\tilde{\gamma}_P > \tilde{\gamma}_R$ and decreases the density $\tilde{\rho}_P < \tilde{\rho}_R$, (b) decreases the surface tension $\tilde{\gamma}_P < \tilde{\gamma}_R$ and increases the density $\tilde{\rho}_P > \tilde{\rho}_R$. The bottom panels display typical spatio-temporal evolution of the product concentration with increasing dimensionless time for systems of length $L_x = 256$, height $L_z = 20$ and (a) $\Delta M = 700$ and $\Delta R = 3$ (b) $\Delta M = -300$ and $\Delta R = -2$ (*cf.* Movies SM1.a and b in the ESI†). The white square ($x_0 - 30$, $3L_z/4$) located in the chemical field of (b) at $t = 1$ identifies the particular position (chosen arbitrarily) at which the concentrations and stream function values are used to build representative time series of the system dynamics. The white arrows illustrate the flow's motion during the formation of an oscillatory cycle. Since the system and the equations are symmetric with respect to the axis $x = x_0$, so is the flow field on either side of the reaction zone.

where the evolution of the chemical concentration fields (eqn (1)–(3)) is coupled to the incompressible Navier–Stokes equations (eqn (4) and (5)) *via* the state equation for the density and surface tension, and the Marangoni boundary condition (eqn (6)) described below. In this set of equations, $T$ is the time, $\boldsymbol{V} = (U, V)$ is the velocity field, $D$ is the molecular diffusion coefficient assumed constant and equal for all species, $P$ is the dynamic pressure, $\mu$ is the constant dynamic viscosity and $g$ is the gravitational acceleration. The Boussinesq approximation is also introduced and implies that density changes only affect the gravitational force term $g\frac{(\rho-\rho_0)}{\rho_0}$.[55] Marangoni boundary conditions (6) are imposed at the free surface to describe the chemically induced shear stress

$$\mu\partial_Z U = \partial_X\gamma, \quad V = 0 \quad \text{at } Z = L_Z. \tag{6}$$

The state equations for the density, $\rho = \rho_0\left(1 + \frac{1}{\rho_0}\sum_I I\partial_I\rho\right)$, and the surface tension, $\gamma = \gamma_0\left(1 + \frac{1}{\gamma_0}\sum_I I\partial_I\gamma\right)$, where $I = A, B, C$ are the dimensional concentrations of the chemical species, are assumed to be linear combinations of the chemical concentrations in diluted solutions, with $\frac{1}{\rho_0}\partial_I\rho$ and $\frac{1}{\gamma_0}\partial_I\gamma$ representing respectively the density and surface tension solutal coefficient of the $I$th species.[56] $\rho_0$ and $\gamma_0$ represent the solvent density and surface tension, respectively. No-flux boundary conditions are imposed for the chemical concentrations at the four boundaries of the reactor, and no-slip conditions are used for the velocity field at the three solid boundaries.

The reaction–diffusion scales for concentration, $A_0$, time, $t_0 = 1/kA_0$, length, $L_0 = \sqrt{Dt_0}$, and the derived scales for velocity, $V_0 = \sqrt{D/t_0}$, and pressure, $P_0 = \mu/t_0$ are used to cast the system in its dimensionless form. The reaction–diffusion scales for density, $\rho' = \frac{\mu}{t_0 L_0 g}$, and surface tension, $\gamma' = \frac{\mu L_0}{t_0}$, are respectively used to define the dimensionless density, $\tilde{\rho} = \frac{\rho-\rho_0}{\rho'} = \sum_i R_i i$, and the dimensionless surface tension, $\tilde{\gamma} = \frac{\gamma-\gamma_0}{\gamma'} = -\sum_i M_i i$ (with $i$ representing the dimensionless concentration of $A$, $B$ and $C$). The dimensionless solutal Rayleigh, $R_i$, and Marangoni, $M_i$, numbers of the $I$th species represent the contribution of each species to the density, ($\partial_I\rho$), and surface tension, ($\partial_I\gamma$), respectively,

and are defined as[30–32]

$$R_i = \frac{\partial_I \rho A_0 L_0^3 g}{D\mu}, \quad (7)$$

$$M_i = -\frac{1}{\mu}\sqrt{\frac{A_0}{kD}}\partial_I \gamma. \quad (8)$$

The equations are then expressed in the stream function–vorticity formulation[57] with the stream function $\psi$ defined such that $u = \partial_z\psi$, $v = -\partial_x\psi$ and vorticity $\omega = \nabla \times \mathbf{v}$. When the reactants have same initial concentrations and identical diffusion coefficients, the conservation of mass implies that $a + b + 2c = 1 \ \forall \ x, z, t$.[30] The final dimensionless RDC equations, in which the lowercase characters represent dimensionless variables, therefore read

$$\partial_t a + \partial_z\psi\partial_x a - \partial_x\psi\partial_z a = \nabla^2 a - ab, \quad (9)$$

$$\partial_t b + \partial_z\psi\partial_x b - \partial_x\psi\partial_z b = \nabla^2 b - ab, \quad (10)$$

$$\partial_t\omega + \partial_z\psi\partial_x\omega - \partial_x\psi\partial_z\omega = S_c(\nabla^2\omega - \Delta R(\partial_x a + \partial_x b)), \quad (11)$$

$$\nabla^2\psi = -\omega, \quad (12)$$

with the Marangoni boundary condition

$$\omega = \Delta M\,(\partial_x a_s + \partial_x b_s) \quad \text{at } z = L_z, \quad (13)$$

where $a_s$ and $b_s$ represent the concentrations at the surface of the reactant solutions A and B, respectively. $S_c = \mu/D\rho_0 = \nu/D$ is the Schmidt number where $\nu = \mu/\rho_0$ is the kinematic viscosity. $S_c$ is set equal to 1000, based on the typical values for the kinematic viscosity $\nu = 0.0089$ cm$^2$ s$^{-1}$ and diffusivity of chemical species $D \sim 10^{-5}$ cm$^2$ s$^{-1}$ in aqueous solutions. $\Delta R$ and $\Delta M$ are defined as, $\Delta R = R - R_c/2$ and $\Delta M = M - M_c/2$, respectively, where $R = R_A = R_B$, $M = M_A = M_B$. $\Delta R$ and $\Delta M$ represent the key parameters to tune the relative importance of solutal buoyancy and surface tension contributions to the convective flows, and thus to control the onset of oscillatory dynamics.

Eqn (9)–(12) are solved numerically with the defined initial and boundary conditions by using an implicit finite difference method, *i.e.* the alternating direction implicit (ADI) method.[58,59] Typical simulations are run over a spatial domain of variable dimensionless length $L_x$ and height $L_z$, discretized over a grid with the integration space steps $h_x = h_z = 0.25$ and the integration time step $h_t = 10^{-5}$.

# 3 Chemo-Marangoni-buoyancy oscillations

Under the conditions considered in this study, reaction–diffusion A + B → C fronts (*i.e.* in the absence of convection) show a symmetrical development of the reaction zone around $x = x_0$.[25] When those fronts are studied in aqueous media, convective flows can be triggered if the reaction induces changes in density ($\Delta R \neq 0$) or in surface tension ($\Delta M \neq 0$). The pure buoyancy-[60] and Marangoni-[61]driven convective cases have shown propagating fronts, and transient oscillatory dynamics have been reported in the latter case for both equal[30] and differential[33] molecular diffusion coefficients.

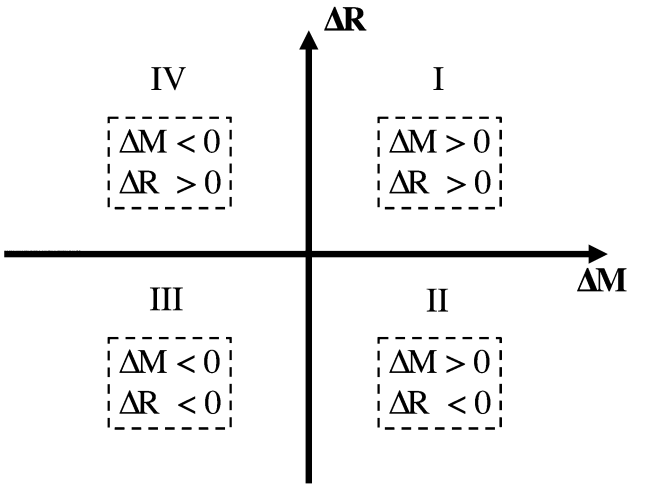


Fig. 2 Classification in a ($\Delta M$, $\Delta R$) parameter plane of the possible interplay between buoyancy- and surface tension-driven flows induced by an A + B → C reaction, for equal diffusion coefficients of all species and equal properties of the reactants. Regions I/III represent antagonistic couplings where the surface tension increases/decreases and the density decreases/increases in the reaction zone. Regions II/IV represent cooperative couplings where both surface tension and density are increased/decreased by the reaction.

Depending on the signs of $\Delta R$ and $\Delta M$, the coupling between buoyancy- and surface-driven flows can be cooperative or antagonistic. In the former, the convection rolls induced by each effect reinforce each other, while the two contributions oppose each other in the latter. The parameter space is therefore divided into 4 regions represented in Fig. 2. When both parameters are of opposite signs, the coupling is cooperative (regions II and IV). In contrast, when both parameters have the same sign, the induced flows are in competition (see Fig. 1) and the coupling is antagonistic (regions I and III). We will focus here on antagonistic cases since the competition between opposite flows has long been known to induce complex dynamics.[30–32,35,38,45]

## 3.1 Phenomenology

Fig. 1a illustrates the previously studied case (region I) where the production of C, less dense than the reactant solutions, generates a vertical upward flow due to gravitational currents and, concurrently, increases the surface tension, thus inducing a vertically downward Marangoni flow.[30–32] In such a case, oscillations occur when $\Delta M$ is beyond a critical threshold, regardless of the value of $\Delta R$.

In the pure chemo-Marangoni case, region I with $\Delta R = 0$, the product C formed at the center of the system $x_0$ is pushed toward the bottom boundary of the system, due to a local increase in the surface tension in the reaction zone, causing the deformation of the concentration field into two symmetrical fronts. The competition between the Marangoni-induced compressive flow and the vertical diffusion relaxation triggers oscillatory dynamics. The addition of buoyancy-driven flows,

 

induced by a local decrease in density in the reaction zone ($\Delta R > 0$), further generates a vertical upward flow, as opposed to the Marangoni-induced contribution, along with two new convective rolls at the bottom of the system, sweeping the product from the reactor's bottom to the surface [Fig. 1a] and reinforcing the vertical diffusive transport, thereby initiating sustained oscillations.[30,31]

In the system studied here (region III), a new type of oscillations can be obtained when the local production of C decreases the surface tension and increases the density ($\Delta M < 0$, $\Delta R < 0$) [Fig. 1b]. In contrast to region I, the Marangoni-driven flow rapidly brings the product to the reactor surface and spreads it laterally toward the borders. In this case, Marangoni-driven convection alone ($\Delta M < 0$, $\Delta R = 0$) is insufficient to observe the emergence of oscillatory dynamics and the only effect is that the product accumulates in the top part of the reactor. When gravitational effects are at play, the denser product layered at the reactor surface by Marangoni forces deforms into sinking fingers [Fig. 1b, $t = 40-80$]. The Marangoni-induced return flow then sweeps the freshly formed fingers toward the center of the system, creating a local accumulation of the product around $x_0$ at the bottom of the system and restoring a situation similar to the initial condition, thereby feeding this wavy dynamics.

Fig. 3 illustrates the temporal evolution of the local concentrations of A and C at a representative point for four distinct cases. It shows that no oscillations are observed in pure chemo-Marangoni-driven dynamics, when the reaction solely decreases the surface tension ($\Delta M = -500$, $\Delta R = 0$). As for the two antagonistic cases described previously (regions I and III), the system can exhibit differences in the oscillation patterns, with the emergence of a bimodal behavior in Region III, illustrated in Fig. 3 for $\Delta M = -500$, $\Delta R = -5$ and detailed in Section 3.2.2. As the reactors are closed, oscillations eventually start to dampen due to the consumption of the reactants and accumulation of the product.

### 3.2 Controlling oscillations

Fig. 4 showcases the oscillatory behavior observed for various $\Delta M$ and $\Delta R$ in region III. In this paper, a dynamical regime is defined as oscillatory when at least two successive minima are present in the temporal evolution of the variables. No oscillatory dynamics are observed in pure-Marangoni or pure-buoyancy systems. A competition between the flows is hence required for oscillations to emerge, in contrast to what was observed in region I. Sustained oscillations are defined as oscillations with quasi-constant amplitudes throughout time (see $\Delta M = -500$, $\Delta R = -5$ in Fig. 3), while oscillations with rapidly decreasing amplitude over time are referred to as damped oscillations (see $\Delta M = -500$, $\Delta R = -0.5$ in Fig. 3). We note that over very long times, all oscillations are eventually damped since the system is a closed one with no inflow of the reactants (and outflow of the products) that would maintain it out of equilibrium.

Sustained oscillations can be observed in an optimal range of $\Delta M$ and $\Delta R$ values. However, when one of the convective effects is predominant, the oscillations start to dampen, and eventually go extinct (see Movies SM2.a and b in the ESI†). This is highlighted in Fig. 4 where sustained oscillations occur for $\Delta R$ values sandwiched between regions of damped oscillations at fixed $\Delta M$. The same is observed at fixed $\Delta R$ when $\Delta M$ is varied. This is in strong contrast with region I where, at fixed $\Delta R$, increasing $\Delta M$ allows to maintain sustained oscillations in the system, provided that $\Delta M$ is above a critical value (Fig. 6 in ref. 31). $\Delta M$ and $\Delta R$ represent thus key parameters to control the dynamics of the system.

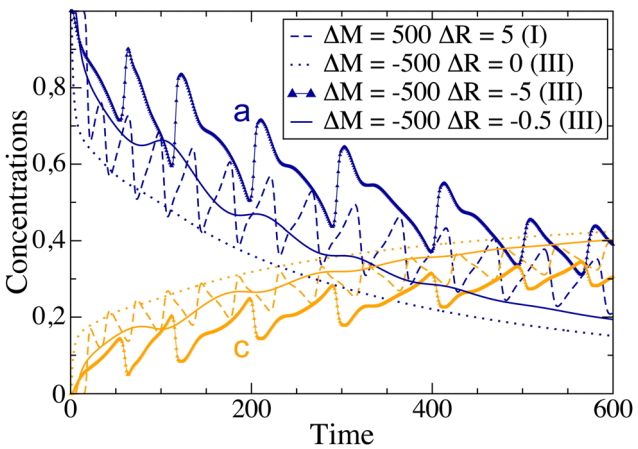


Fig. 3 Local time series of the concentrations $a$ and $c$ at a representative point of the system ($x_0 - 30$, $3L_z/4$) ($L_z = 20$ and $L_x = 256$). The blue and orange curves represent the evolution of species A and C, respectively. The dashed curves represent a typical system in region I, the dotted curves represent a purely chemo-Marangoni system in region III, the curves with triangles represent a typical sustained oscillatory system of region III and the continuous curves represent a typical damped oscillatory system of region III.

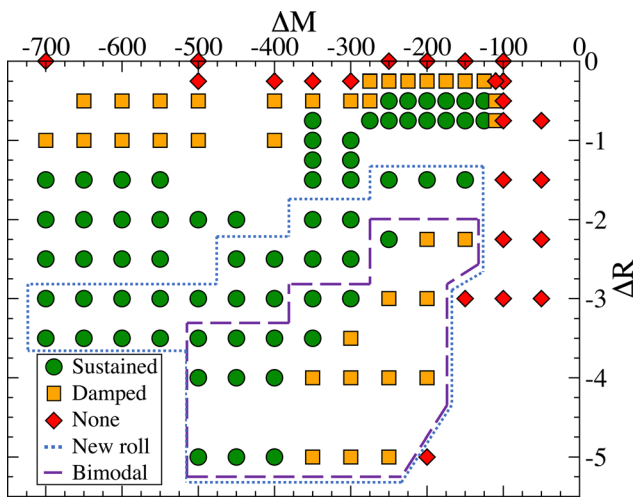


Fig. 4 Classification of the dynamical regimes characterizing region III (where the reaction decreases the surface tension, $\Delta M < 0$, and increases the density, $\Delta R < 0$) of the parametric space diagram ($\Delta M$, $\Delta R$) ($L_z = 20$ and $L_x = 256$). Oscillations with quasi-constant amplitudes throughout time are defined as sustained, whereas oscillations with rapidly decreasing amplitude over time are referred to as damped oscillations. The blue dotted polygon includes the systems in which new convective rolls emerge in time, and the purple dashed polygon includes the systems presenting a bimodal behavior. We note that for higher $|\Delta M|$, the oscillations are damped and eventually disappear.

The phenomenology described above suggests that oscillations are also critically sensitive to the system length ($L_x$) and the height ($L_z$). We therefore explore the influence of $\Delta M$, $\Delta R$, $L_z$ and $L_x$ on the occurrence of oscillatory instabilities as well as on the type of oscillatory behavior (either sustained or damped), the oscillation period and frequency, and the fluid velocities.

**3.2.1 Role of $\Delta M$.** It was shown that, in the antagonistic mechanism characterizing region I, $\Delta M$ plays a key role in the onset of oscillatory dynamics. When the reaction increases the surface tension sufficiently ($\Delta M > \Delta M_{crit} > 0$), the system can undergo oscillatory instabilities.

Even though oscillatory behaviors are not observed in the pure chemo-Marangoni case studied here [Fig. 4 when $\Delta R = 0$], $\Delta M$ represents an important parameter for the control of the oscillatory properties when both buoyancy- and Marangoni-driven contributions are at play. As shown in Fig. 5, illustrating the evolution in time of the stream function for different values of $\Delta M$ at constant $\Delta R$, an increase in $|\Delta M|$ allows the apparition of oscillations and increases their amplitude. $\Delta M$ also controls the frequency of these spatio-temporal oscillations: as $|\Delta M|$ increases, a maximum frequency is reached, due to a more rapid Marangoni convective motion. A further increase in $|\Delta M|$ causes the strengthening of Marangoni-driven convective rolls, subsequently weakening the flow competition and thus the oscillation's frequency (Fig. 5).

By increasing $|\Delta M|$ we can thus modulate the dynamical regime, following the sequence no-oscillations → damped → sustained → damped → no-oscillations. This transition scenario is different from the one observed in region I (Fig. 6 in ref. 31), where sustained oscillations are not damped by an increase in $\Delta M$.

**3.2.2 Role of $\Delta R$.** The local values of the stream function at a representative point are reported as a function of time in Fig. 6 for different values of $\Delta R$ (with $\Delta M$ fixed). It can be seen how increasing $|\Delta R|$ first induces the onset of oscillatory behaviors and eventually leads to their dampening. As we have shown by varying $\Delta M$, we can modulate the type of dynamical regimes by tuning $|\Delta R|$ (Fig. 4). For instance, beyond a certain value of $|\Delta R|$, the system can exhibit bimodal oscillations. The changes in the dynamics when varying $\Delta R$ can be related to the extent of the buoyancy-driven fingers rich in the reaction product.

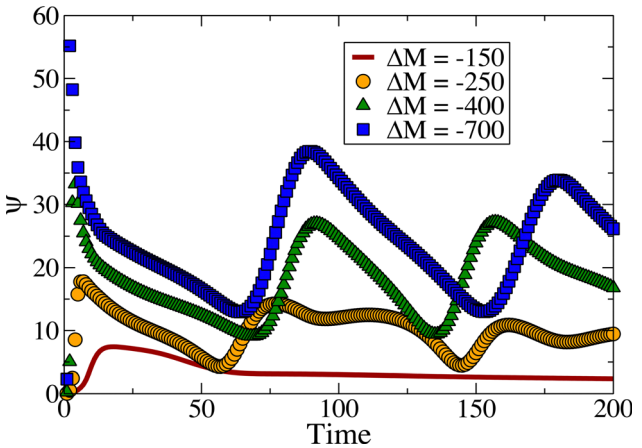


Fig. 5 Local time series evolution of the stream function ($\psi$) at a representative point of the system ($x_0 - 30$, $3L_z/4$) at constant $\Delta R = -3$ for four different values of $\Delta M$ with $L_z = 20$ and $L_x = 256$.

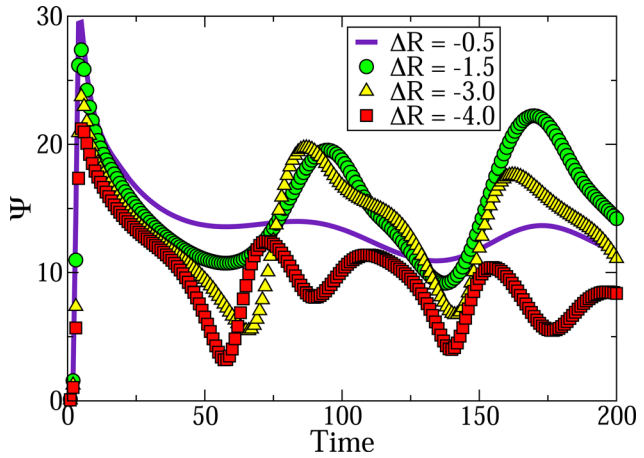


Fig. 6 Local time series evolution of the hydrodynamic field ($\psi$) at a representative point of the system ($x_0 - 30$, $3L_z/4$) at constant $\Delta M = -300$ for different values of $\Delta R$ with $L_z = 20$ and $L_x = 256$.

On the one hand, increasing $|\Delta R|$ strengthens the buoyancy-driven flows and, in turn, the length of the fingers emerging close to the surface [Fig. 1b since $t = 40$] increases up to a value of $|\Delta R|$ beyond which they can reach the bottom of the reactor.

On the other hand, the larger the $|\Delta R|$, the larger the amount of denser product C located at the reactor's bottom boundary. At a certain value of $|\Delta R|$, both effects start interacting, leading to a new set of convective rolls.

The apparition of these rolls is emphasized in Fig. 7 (right), displaying the vertical velocity fields for $\Delta M = -300$, $\Delta R = -4$ at specific times and illustrating the interaction of the fingers with the product located at the bottom. The system evolves over time with the emergence of fingers created at the surface and reaching the bottom of the reactor. The product C pushed toward the reactor's bottom due to the main buoyancy-driven convection roll is also spread laterally along the bottom boundary, enabling its interaction with the fingers. This interaction is followed by the emergence of a new counter-rotating convective roll (red arrow at $t = 90$).

As the system evolves, the new convective roll grows ($t = 120$) and utterly merges with the initial buoyancy-driven convection roll ($t = 130$). As a result, the Marangoni-driven return flow (black circle at $t = 90$) is split into two distinct rolls ($t = 150$), responsible of the second extremum in the bimodal oscillatory cycle. Fig. 7 (left) illustrates the case where new convective rolls are absent, leading to unimodal oscillatory dynamics.

It can be noted that convective rolls are also formed at the bottom of the reactor for high $|\Delta M|$ and lower $|\Delta R|$ (*cf.* Fig. SF1 in the ESI†), but no bimodal oscillations are observed in this case, as the initial buoyancy-driven convective roll is located far from the new roll and there is no interaction between them.

**3.2.3 Role of $L_z$.** For the chemohydrodynamic mechanism described in region I (reactions increasing the surface tension

 

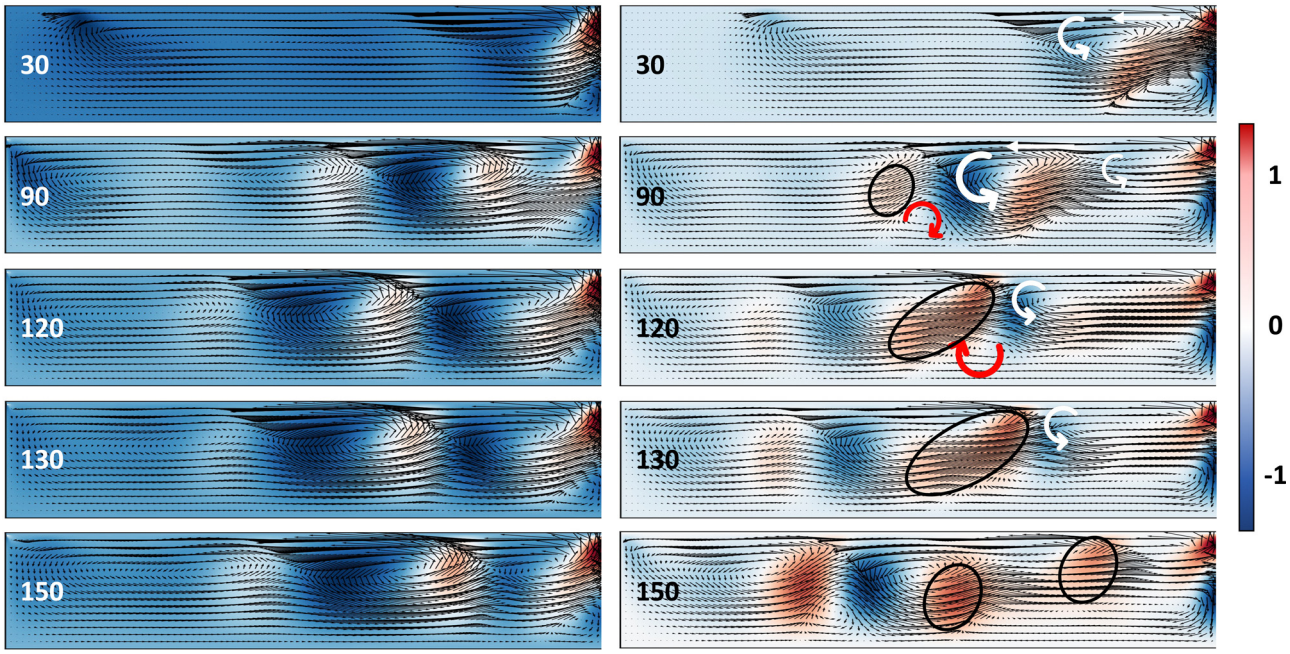


Fig. 7 Snapshots of the spatio-temporal evolution of the vertical velocity ($v$) fields with increasing dimensionless time for (left) unimodal oscillations at $\Delta M = -300$ and $\Delta R = -1.5$, (right) bimodal oscillations at $\Delta M = -300$ and $\Delta R = -4$. The red arrows represent the newly merged convective rolls and the black circles highlight the separation of a convective roll. The red/blue zones represent the zones of maximum/minimum vertical velocity. The snapshots are displayed in a semi-system (from $L_x = 0$ to $L_x/2$) since the system is symmetric around $x = L_x/2$. The complete spatio-temporal evolutions of the vertical velocity and of the concentration field are displayed in Movies SM3.a, b and SM3.c, d, respectively, in the ESI.†

and decreasing the density), it was found that $L_z$ can control the buoyancy-driven convection, the relative timescales of the antagonistic Marangoni-driven and reaction–diffusion/buoyancy-driven flows and, as a consequence, the critical threshold of $\Delta M$ beyond which oscillations can be observed.[30,31]

Similarly, in region III (reactions decreasing the surface tension and increasing the density), for low $L_z$ values, no oscillations are observed, as surface-driven flows dominate the system dynamics (Fig. 8). A progressive increase in the height of the system contributes to counterbalance Marangoni-driven convection emerging at the surface by increasing the space available to the buoyancy-driven contribution needed to trigger spatio-temporal oscillations.

Fig. 8 represents the oscillatory dynamics observed at fixed $L_x$ and $\Delta R$ for various sets of $\Delta M$ and $L_z$ values. The pattern of the dynamical regimes accessible to the system and the route from non-oscillatory to oscillatory conditions is similar to the one observed in the ($\Delta M$, $\Delta R$) parametric space diagram represented in Fig. 4. This general arrangement remains qualitatively preserved for variable values of $\Delta R$, though by decreasing $|\Delta R|$, the $|\Delta M|_{\min}$ value for which oscillations occur also decreases.

The influence of $L_z$ on the system dynamics is further illustrated in Fig. 9, showcasing the oscillation period, $\tau$, as a function of $L_z$, for various $\Delta M$ at fixed $\Delta R$. The period is defined as the dimensionless time interval between global maxima (or minima) of successive oscillations. As mentioned above, below a minimal threshold $L_z$, no oscillatory dynamics emerge. Then the period increases with $L_z$ up to a maximum value beyond which a sharp decrease occurs (due to a change of regime, as explained below), followed by a second increase.

The new convective rolls, described in the previous section, form when a critical maximum value of $L_z$ is reached. Beyond that value, oscillations are bimodal and damped accompanied by a sharp decrease in the period. As $L_z$ is further increased (with $\Delta M$ and $\Delta R$ fixed) the period grows again.

Notably, although beyond a certain critical maximum $L_z$ only damped oscillations are observed, the oscillatory phenomenon

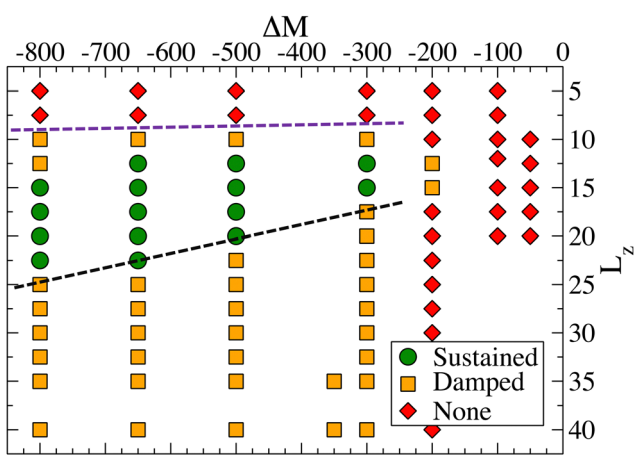


Fig. 8 Classification of dynamical regimes in the parametric space diagram ($\Delta M$, $L_z$) with $\Delta R = -5$ and $L_x = 256$. The purple and black dashed lines represent the critical minimum $L_z$ beyond which oscillatory dynamics occur, and the critical maximum $L_z$ beyond which bimodal oscillations are observed, respectively. By further increasing $L_z$, the bimodal oscillations remain damped.

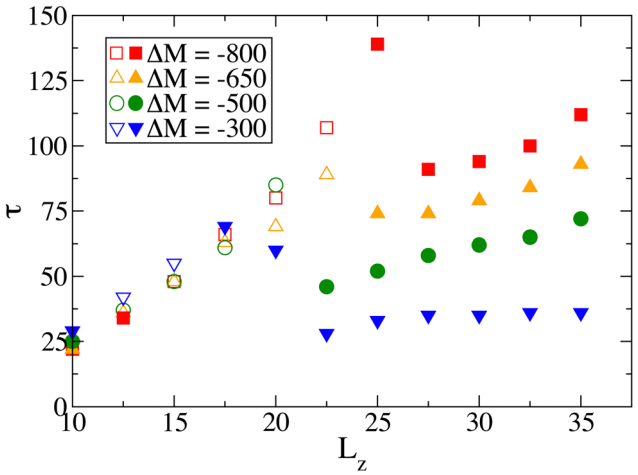


Fig. 9 Characterization of the oscillation period, $\tau$, as a function of the system height, $L_z$, for different values of $\Delta M$ at a fixed value of $\Delta R = -5$. Filled symbols correspond to systems presenting damped oscillations and empty symbols correspond to sustained oscillations.

persists despite a further increase of $L_z$ (Fig. 8). This constitutes a major difference with the previously studied dynamics of region I, in which Budroni *et al.* highlighted a maximum $L_z$ value beyond which oscillations are suppressed (see Fig. 10 in ref. 31).

The trends $\tau(L_z)$ for different values of $\Delta M$ are similar, though the critical height at which the maximum/minimum oscillation periods occur varies. In fact, systems presenting stronger Marangoni-driven flows at the surface need to be counterbalanced by stronger downward flows, which is intensified (at fixed $\Delta R$) by higher values of $L_z$.

Our analysis confirms that, according to what we observed for region I, varying $L_z$ has a similar effect as varying $\Delta R$, since both parameters control the intensity of buoyancy-driven flows and the characteristic size of related convective rolls. Furthermore, by increasing the height of the system, we shift the apparition of the bimodal oscillatory regime toward larger $|\Delta R|$ by increasing the space between the fingers located at the top of the system and the denser product accumulated at the bottom of the system.

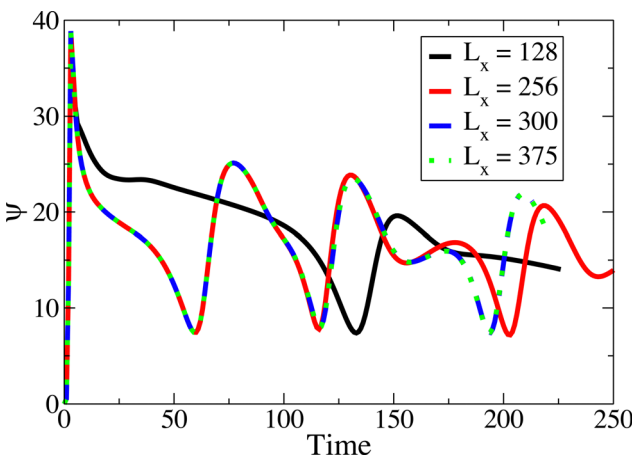


Fig. 10 Local time series of the hydrodynamic field ($\psi$) at a representative point of the system ($x_0 - 30$, $3L_z/4$) at constant $\Delta R = -5$, $\Delta M = -500$ and $L_z = 20$ for four different $L_x$. For this set of parameters, the onset of oscillatory dynamics occurs for values of $L_x$ located between 100 and 128.

**3.2.4 Role of $L_x$.** Spatiotemporal oscillations of region I were shown to be essentially independent of the length of the system, since the core of the underlying mechanism is localized at the center of the reactor (*cf.* Fig. 1a).[31]

On the other hand, chemo-Marangoni-buoyancy scenarios of region III occur when the fingered product C is pushed toward the center of the system by the return flow, which extent and morphology are strongly affected by the position of the lateral borders.

This suggests that $L_x$ can play a critical role in the development and control of spatio-temporal oscillations. Indeed, we found a minimum length, $L_x^{\min}$, (which value depends upon $\Delta M$ and $\Delta R$, *e.g.* $L_x^{\min}$ is located between 100 and 128 for $\Delta R = -5$ and $\Delta M = -500$) below which the oscillatory instability does not develop.

Fig. 10 shows the temporal evolution of the stream function at a specific position ($x_0 - 30$, $3L_z/4$) for different systems lengths. We can appreciate how, as long as $L_x > L_x^{\min}$, oscillatory systems behave identically at shorter times and differentiate from each another only when the influence of the lateral borders can be felt at the considered position. Indeed, when the product C reaches the lateral boundaries, it is reflected back toward the center of the system, diminishing the intensity of the original flow and increasing the oscillation period, as reported in Fig. 10. Since the numerical simulations are performed in closed systems, these oscillations are slowly dampening due to the accumulation of the product C in the system. We note that this dampening of oscillations arises from the closed nature of our system and is distinct from that defined in Fig. 4, which is intrinsic to the dynamics.

## 4 Conclusions

In this work, we have presented a new mechanism for the emergence of oscillatory dynamics in simple bimolecular reactions when chemically driven antagonistic Marangoni- and buoyancy-driven convection are at play. In contrast to a previously observed antagonistic scenario (region I), spatio-temporal oscillations cannot be driven by pure Marangoni- or buoyancy-driven flows. Key to the emergence of these behaviors is the competition of both contributions to the flow. Oscillations develop in the form of fingers of product C sinking from the surface of the reactor and pushed to its center by a lateral return flow.

By varying key parameters, it is possible to control the oscillatory regimes, shifting from damped to sustained oscillations. As one convective effect becomes dominant over the other, a quenching of oscillations is observed.

We have showed that varying $|\Delta M|$ (thus modulating the changes in surface tension due to the reaction), not only controls the onset of oscillatory dynamics, but also their characteristic amplitude and the oscillations frequency.

A particularly interesting feature, so far unseen in the A + B → C systems, has been observed by increasing the buoyancy contribution $|\Delta R|$. The latter has two distinct roles: larger $|\Delta R|$ values strengthen the buoyancy-driven flows, thus the extent of the fingers of product formed close to the surface, and increase the amount of product C located at the reactor's bottom boundary. When the fingers start to interact with the product accumulated at the bottom of the reactor, a new convective motion opposed to the initial one is created and bimodal oscillations develop. Further increasing the magnitude of this parameter does not induce any period doubling sequence to chaos.

The variation of the height of the system $L_z$ shows a similar impact on the dynamics as the variation of $\Delta R$, since both parameters control the importance of buoyancy-driven convection. We have highlighted the existence of critical minimum and maximum values of the reactor's height needed for oscillatory instabilities.

Finally, the length of the system $L_x$ has also been characterized as a critical parameter, as the system needs to be long enough ($L_x^{\min}$) to observe the development of the wavy dynamics.

This work proposes a further step in the way of designing chemical self-induced oscillations in simple reactions, here exploiting chemohydrodynamics. This approach can considerably enlarge the number of chemical systems where complex behaviors can be induced or controlled if undesired. In particular, we have shown that the antagonistic coupling between orthogonally oriented surface- and buoyancy-driven flows can be identified as a general source of oscillatory instabilities that, similar to classical chemical oscillators, relies on a fast activation phase (here played by the chemically driven Marangoni flows) and a slow oppositely-oriented relaxation phase (here the buoyancy contribution).

In this first minimal approach, we have considered conditions that allow for spatio-temporal pulsations symmetric with respect to the reactor center. From the perspective of an experimental implementation and validation of these phenomena, our theoretical framework should consider general reactants with different properties (like diffusivities, densities, *etc.*), which can result in more complex and asymmetric traveling structures. However, our preliminary results in this direction suggest that the main features and trends found for the symmetric scenarios are preserved.

## Conflicts of interest

There are no conflicts to declare.

## Acknowledgements

We acknowledge the Université libre de Bruxelles (ULB) and Fondation ULB for financial support.

## Notes and references

1 G. Nicolis and I. Prigogine, *Self-Organization in Nonequilibrium systems*, Wiley, New York, 1977.
2 R. Lefever, G. Nicolis and P. Borckmans, *J. Chem. Soc., Faraday Trans. 1*, 1988, **84**, 1013–1023.
3 P. Gray and S. K. Scott, *Chemical Oscillations and Instabilities. Non-linear Chemical Kinetics*, Oxford University Press, Oxford, UK, 1994.
4 I. R. Epstein and J. A. Pojman, *Introduction to Nonlinear Chemical Dynamics: Oscillations, Waves, patterns and Chaos*, Oxford University Press, New York, 1994.
5 R. J. Field and M. Burger, *Oscillations and traveling waves in chemical systems*, John Wiley and Sons, New York, 1985.
6 W. Bray and H. Liebhafsky, *J. Am. Chem. Soc.*, 1931, **53**, 38–44.
7 B. Belousov, *Sbornik Referatov po Radiatsionni Meditsine*, 1958, pp. 145–147.
8 A. Goldbeter and M. J. Berridge, *Biochemical Oscillations and Cellular Rhythms: The Molecular Bases of Periodic and Chaotic Behaviour*, Cambridge University Press, 1996.
9 J. D. Murray, *Mathematical Biology: I. An Introduction*, Springer New York, 2002, vol. 17.
10 R. Yoshida, *Adv. Mater.*, 2010, **22**, 3463–3483.
11 A. Isakova and K. Novakovic, *J. Mater. Chem. B*, 2018, **6**, 5003–5010.
12 T. Geher-Herczegh, Z. Wang, T. Masuda, R. Yoshida, N. Vasudevan and Y. Hayashi, *Macromolecules*, 2021, **54**, 6430–6439.
13 G. P. Misra and R. A. Siegel, *J. Controlled Release*, 2002, **79**, 293–297.
14 I. Z. Kiss, Y. Zhai and J. L. Hudson, *Science*, 2002, **296**, 1676–1678.
15 V. K. Vanag, *Chaos*, 2019, **29**, 033106.
16 M. A. Budroni, K. Torbensen, O. L. Pantani, S. Ristori, F. Rossi and A. Abou-Hassan, *Chem. Commun.*, 2020, **56**, 11771–11774.
17 M. A. Budroni, K. Torbensen, S. Ristori, A. Abou-Hassan and F. Rossi, *J. Phys. Chem. Lett.*, 2020, **11**, 2014–2020.
18 M. A. Budroni, G. Pagano, D. Conte, B. Paternoster, R. Dambrosio, S. Ristori, A. Abou-Hassan and F. Rossi, *Phys. Chem. Chem. Phys.*, 2021, **23**, 17606–17615.
19 D. Przyczyna, P. Zawal, T. Mazur, P. L. Gentili and K. Szacilowski, *Jpn. J. Appl. Phys.*, 2020, **59**, 050504.
20 A. Bose and J. Gorecki, *Front. Chem.*, 2022, **10**, 16.
21 K. Gizynski and J. Gorecki, *Phys. Chem. Chem. Phys.*, 2017, **19**, 28808–28819.
22 M. A. Budroni, S. Garroni, G. Mulas and M. Rustici, *J. Phys. Chem. C*, 2017, **121**, 4891–4898.
23 P. L. Gentili, M. Dolnik and I. R. Epstein, *J. Phys. Chem. C*, 2014, **118**, 598–608.
24 J. Horváth, *Polymer*, 2015, **79**, 243–254.
25 L. Gálfi and Z. Rácz, *Phys. Rev. A: At., Mol., Opt. Phys.*, 1988, **38**, 3151–3154.
26 Z. Jiang and C. Ebner, *Phys. Rev. A: At., Mol., Opt. Phys.*, 1990, **42**, 7483–7486.
27 Y. E. L. Koo and R. Kopelman, *J. Stat. Phys.*, 1991, **65**, 893–918.
28 H. Taitelbaum, Y.-E. L. Koo, S. Havlin, R. Kopelman and G. H. Weiss, *Phys. Rev. A: At., Mol., Opt. Phys.*, 1992, **46**, 2151–2154.

29 R. Tiani and L. Rongy, *Phys. Rev. E*, 2019, **100**, 030201.
30 M. A. Budroni, V. Upadhyay and L. Rongy, *Phys. Rev. Lett.*, 2019, **122**, 244502.
31 M. A. Budroni, A. Polo, V. Upadhyay, A. Bigaj and L. Rongy, *J. Chem. Phys.*, 2021, **154**, 114501.
32 M. A. Budroni, F. Rossi and L. Rongy, *ChemSystemsChem*, 2021, **4**, e202100023.
33 R. Tiani and L. Rongy, *Front. Phys.*, 2022, **10**, 860419.
34 A. De Wit, K. Eckert and S. Kalliadasis, *Chaos*, 2012, **22**, 037101.
35 R. Tiani, A. De Wit and L. Rongy, *Adv. Colloid Interface Sci.*, 2018, **255**, 76–83.
36 A. von Kameke, F. Huhn, A. P. Muñuzuri and V. Pérez-Muñuzuri, *Phys. Rev. Lett.*, 2013, **110**, 088302.
37 S. Mukherjee and M. R. Paul, *Phys. Rev. E*, 2020, **101**, 032214.
38 S. Mukherjee and M. R. Paul, *J. Fluid Mech.*, 2022, **942**, A36.
39 L. Rongy and A. De Wit, *J. Chem. Phys.*, 2009, **131**, 184701.
40 L. Rongy, P. Assemat and A. De Wit, *Chaos*, 2012, **22**, 037106.
41 I. Nagypal, G. Bazsa and I. R. Epstein, *J. Am. Chem. Soc.*, 1986, **108**, 3635–3640.
42 J. A. Pojman and I. R. Epstein, *J. Phys. Chem.*, 1990, **94**, 4966–4972.
43 L. Rongy, G. Schuszter, Z. Sinkó, T. Tóth, D. Horváth, A. Tóth and A. De Wit, *Chaos*, 2009, **19**, 023110.
44 D. Horváth, M. A. Budroni, P. Bába, L. Rongy, A. De Wit, K. Eckert, M. J. B. Hauser and A. Tóth, *Phys. Chem. Chem. Phys.*, 2014, **16**, 26279–26287.
45 M. A. Budroni, L. Rongy and A. De Wit, *Phys. Chem. Chem. Phys.*, 2012, **14**, 14619–14629.
46 K. I. Agladze, V. I. Krinsky and A. M. Pertsov, *Nature*, 1984, **308**, 834–835.
47 M. A. Budroni, M. Masia, M. Rustici, N. Marchettini and V. Volpert, *J. Chem. Phys.*, 2009, **130**, 024902.
48 M. A. Budroni, I. Calabrese, Y. Miele, M. Rustici, N. Marchettini and F. Rossi, *Phys. Chem. Chem. Phys.*, 2017, **19**, 32235–32241.
49 D. M. Escala, M. A. Budroni, J. Carballido-Landeira, A. De Wit and A. P. Muñuzuri, *J. Phys. Chem. Lett.*, 2014, **5**, 413–418.
50 M. A. Budroni and A. De Wit, *Chaos*, 2017, **27**, 104617.
51 M. A. Budroni, L. Lemaigre, D. M. Escala and A. De Wit, *Langmuir*, 2022, **39**, 997–1009.
52 O. E. Shklyaev, V. V. Yashin, S. I. Stupp and A. C. Balazs, *Commun. Phys.*, 2020, **3**, 1–9.
53 P. L. Gentili, M. S. Giubila and B. M. Heron, *ChemPhysChem*, 2017, **18**, 1831–1841.
54 P. L. Gentili, M. S. Giubila, R. Germani and B. M. Heron, *Dyes Pigm.*, 2018, **156**, 149–159.
55 D. Tritton, *Physical Fluid Dynamics*, Clarendon Press, 1988.
56 P. Cheng, M. Bestehorn and A. Firoozabadi, *Water Resour. Res.*, 2012, **48**, 10902.
57 E. Guyon, J. Hulin, L. Petit and C. Mitescu, *Physical Hydrodynamics*, Oxford University Press, 2015.
58 D. W. Peaceman and H. H. Rachford, *J. Soc. Ind. Appl. Math.*, 1955, **3**, 28–41.
59 C. Fletcher and K. Srinivas, *Computational Techniques for Fluid Dynamics 1*, Springer, Berlin, Heidelberg, 1991.
60 L. Rongy, P. Trevelyan and A. De Wit, *Phys. Rev. Lett.*, 2008, **101**, 084503.
61 R. Tiani and L. Rongy, *J. Chem. Phys.*, 2016, **145**, 124701.


 